,

University of Padova

Department of Physics and Astronomy Department "Galileo Galilei"

Master Thesis in Nuclear Physics

Study of the $^{13}C(p,\gamma)^{14}N$ reaction at the Felsenkeller laboratory

Supervisor
Prof. Antonio Caciolli
University of Padova

Co-supervisor
Dr. Jakub Skowronski
University of Padova

Master Candidate
Mohammad Nusir

Student ID
2097637

Academic Year
2023-2024

This thesis is dedicated to my loving parents, whose unwavering support, encouragement, and sacrifices have been my guiding light throughout my academic journey. Your belief in me has been my greatest strength.

To my family, thank you for always being there, and providing me with laughter and perspective when I needed it the most.

To my mentor and advisor, your invaluable guidance and insight have been instrumental in the completion of this work. Your dedication to my success has been a source of inspiration.

To my friends, thank you for your understanding and support, for the countless discussions, and for always being there to cheer me on.

Lastly, to all those who have contributed to my academic and personal growth, your influence has shaped me into who I am today. This work is a testament to your impact on my life.

With heartfelt gratitude,

Abstract

The $^{13}C(p,\gamma)^{14}N$ reaction takes part in the CNO cycle, which is the primary hydrogen-burning process in massive stars and the hydrogen-burning shells of Red Giant Branch (RGB) and Asymptotic Giant Branch (AGB) stars, with temperatures ranging from 0.02 to 0.1 GK. As a catalytic cycle, the CNO reactions not only transform four protons into a helium nucleus but also regulate the abundances of carbon, nitrogen, and oxygen isotopes. Specifically, the $^{12}C/^{13}C$ ratio serves as a sensitive marker of stellar nucleosynthesis and mixing processes, making it a valuable tool for tracing the chemical evolution of the Galaxy.

Measurements of the $^{13}C(p,\gamma)^{14}N$ reaction cross section performed at the Felsenkeller underground facility in Dresden (Germany) in the energy range 350-700 keV, Being located underground, the cosmic ray background is suppressed by 99%, thus providing a unique environment for low-energy measurements of reaction cross sections. The prompt γ-rays linked to the formation of the ^{14}N nuclide were analyzed to determine the reaction cross section and the resulting S-factor was then compared with those from previous studies.

The $^{12}C/^{13}C$ ratio derived from this study and the obtained reaction rates can greatly enhance our ability to model and understand the mixing phenomena occurring in stars. The improved precision allows for better constraining of theoretical stellar models against observations, resulting in more accurate predictions of stellar evolution and nucleosynthesis processes.

Contents

Listing of figures

1 Introduction

The research in Nuclear Astrophysics is of fundamental importance to understand the origin of all the elements in our Universe. It focuses on studying the intricate nuclear reaction networks that are responsible of creating nuclei heavier than H and that drives the stellar evolution. Stars are the main blacksmith of our Universe that not only produce energy necessary for life on Earth, but also creates more and more complex elements inside their cores that make up everything in our Universe. Thus, by knowing rates of these reactions inside stellar interiors it is possible to study the evolution of our Universe.
In this chapter the main concepts of stellar evolution will be illustrated, focusing on two different types of stars that are particularly prolific in terms of nucleosynthesis. Then the main ingredients of the reaction mechanism inside the stars will be explained. Finally, the reaction under study, namely the $^{13}C(p,\gamma)^{14}N$ will be described and the state of the art discussed.

1.1 Stellar Evolution

Hydrogen and helium are still the most abundant elements in our Universe. Most of these are located in the interstellar medium in form of an interstellar nebula. This could be created either from the nuclei directly coming from the Big Bang itself or from the remnants of an already-dead star. When the amount of elements is big enough, the gravitational force starts to compress all the nuclei, which as a consequence increases their kinetic energy and thus the temperature. When the density and the energy of the nuclei is high enough, the first fusion

reaction is ignited and the star is born.

The pp chain is dominant in primary generation stars with M 1.5 $M_{\odot}$ and a core temperature lower than 20 MK [3]. The scheme of the process as it takes place in the Sun is shown in Figure 1.1. In the pp chain, four hydrogen nuclei (protons) are fused into one helium nucleus through a series of reactions. This process releases energy in the form of gamma rays and neutrinos.

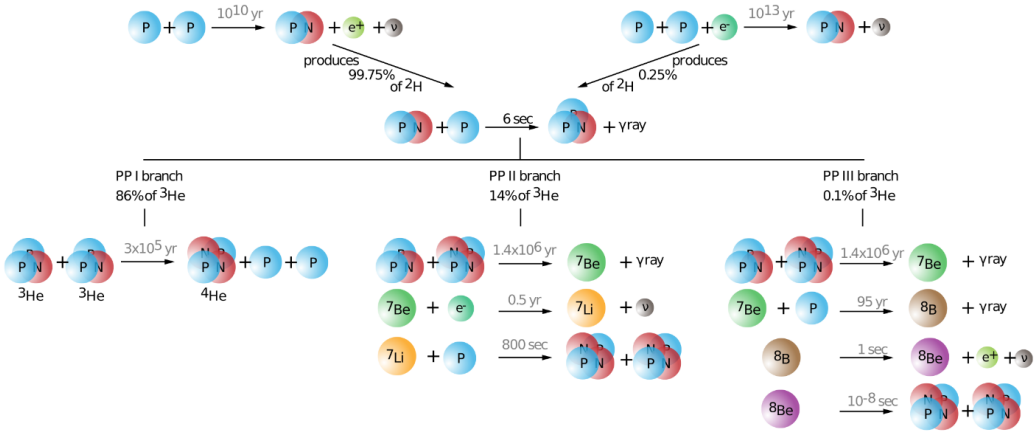

Figure 1.1: Scheme of the pp chain reactions, multiple chains are possible depending on the stellar temperatures.

An alternative for the pp process is the CNO cycle. It consists of several reactions on C, N and O nuclei that cathalitically create one ^{4}He nucleus from 4^{1}H. The entire cycle can be seen in Figure 1.2. This is the predominant mechanism of the hydrogen burning for stars with masses approximately 1.5 higher than the solar one [3]. Nevertheless, the star composition must contain some of the nuclei that takes part in it. This propriety is called metallicity, ie. how many nuclei heavier than ^{1}H and ^{4}He does the star contain. As an example, the first generation stars, created just after the Big Bang, have very low metallicity, since no C, N nor O nuclei were produced before. Thus these, even with high enough mass, can not burn the hydrogen through the CNO cycle. Additionally, the cycle is important for the nucleosynthesis: the amounts of each isotope is changed when the cycle is ignited and reaches an equilibrium value given by the reaction rates of each of the reactions.

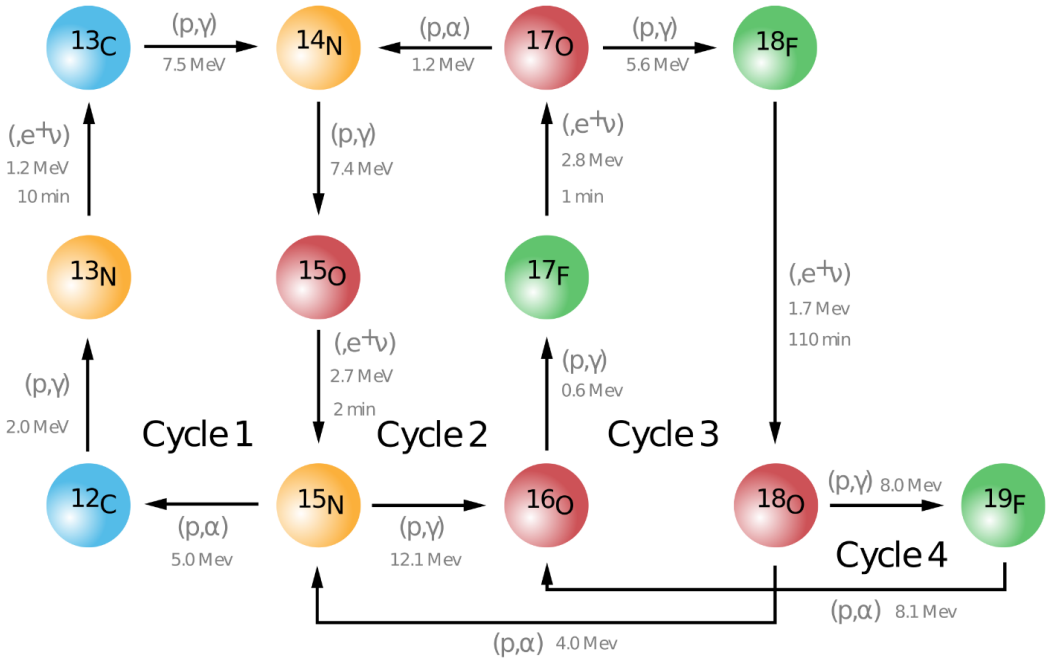

Figure 1.2: Complete scheme of CNO cycles.

Once most of the hydrogen has been burned the star is not able to sustain itself. The hydrogen-burning region is pushed towards the outer shell of the star, leaving the core made of helium. The stars thus begin to expand and cool while the core is being contracted and enters into the Red Giant Branch (RGB) phase. At this point, the first dredge-up (FDU) occurs [4]. The convective motion penetrates into the hydrogen-burning regions of the star and brings up heavier elements, such as carbon and nitrogen, from the stellar core to the surface. As a result of FDU, the surface elemental abundances of the star change. The newly mixed material, enriched hydrogen burning products, is transported to the stellar surface, where it can be observed through spectroscopic analysis. This alteration of surface composition is an important aspect of stellar evolution and has implications for the chemical enrichment of the interstellar medium and the formation of subsequent generations of stars and planetary systems.

When the high enough temperature is reached in the core, the helium burning can be started inside the core which will permit the star to produce energy again. The process consists of triple ^{4}He reactions that create ^{12}C nuclei [3]. This process is highly unlikely due to being a three-body process: first, the ^{8}Be nucleus must be produced, which is unstable with a half-life of $8.19 \times 10^{17} s$, and then has to capture a ^{4}He nucleus before decaying. Nevertheless, this process

is favoured by the existence of the Hoyle state in the ^{12}C nuclei [3].

Once the star has exhausted most of its helium, the process called second dredge up (SDU) occurs [4], which is analogous to the FDU: the convective envelope penetrates in the helium-burning regions. It brings up all the produced elements to the stellar surface.

At this evolutionary point, the star usually enters its most prolific stage for nucleosynthesis: the Asymptotic Giant Branch (AGB) [4]. The stars once again expands and cools, leaving a core made of carbon and oxygen, the products of the helium burning. The helium burning starts again in a shell around the core, until the helium is mostly exhausted. At this point, the hydrogen burning starts in a thin shell around the helium one. At a certain point, when the helium builds up significantly from the hydrogen-burning shell, the helium burning ignites again. This process is known as helium flash and it repeats several times during the following star evolution. The hydrogen and helium shells are constantly switched off and on up until most of the hydrogen is burned and it can no longer provide helium for the other shell.

In the meantime, the phenomenon called third dredge up (TDU) occurs several times. When the hydrogen shell is switched off, the convective motion can pene- trate down to the helium burning region and thus brings up all the encountered material up to the surface, enriching the surface with the helium burning products and several other elements [4]. A simplified scheme of the TDU is shown in Figure 1.3. The TDU is thus responsible for the creation of carbon stars. Carbon stars are giant stars with a surfaces carbon abundance higher than the oxygen one, resulting from the dredge up of carbon-rich material from the helium burning ashes. These carbon stars are particularly interesting to astronomers because they play a crucial role in the chemical enrichment of the universe. Additionally, the AGB start pulsation can trigger intense mass loss in the star [5]. As the convective envelope reaches deeper layers and brings up the hot material from the deeper region, it becomes unstable leading to the ejection of stellar material in the form of stellar winds that then enrich the interstellar medium.

Once the AGB star finishes most of its helium and hydrogen, and thus is not able to maintain the burning in its shells, two fates are possible. Either the star mass is big enough to start the process of carbon burning, or it dies as a White Dwarf, ie. hot stellar core remnant made of carbon and oxygen unable to undergo further fusion processes. If the star mass is approximately $> 8M_{\odot}$, the $^{12}C + ^{12}C$ fusion starts inside the stellar core. At this point the star evolution is

quick and straightforward respect to the previous stages, producing heavier and heavier nuclei: once the ^{12}C has been depleted, the neon burning phase starts, followed by the oxygen burning and the silicon burning phases. When the iron has been reached, the star is not able anymore to produce any energy since the fusion processes starts to be endothermic and the stellar core inevitably collapses, exploding in the supernova and leaving either a Neutron Star or a Black Hole [3].

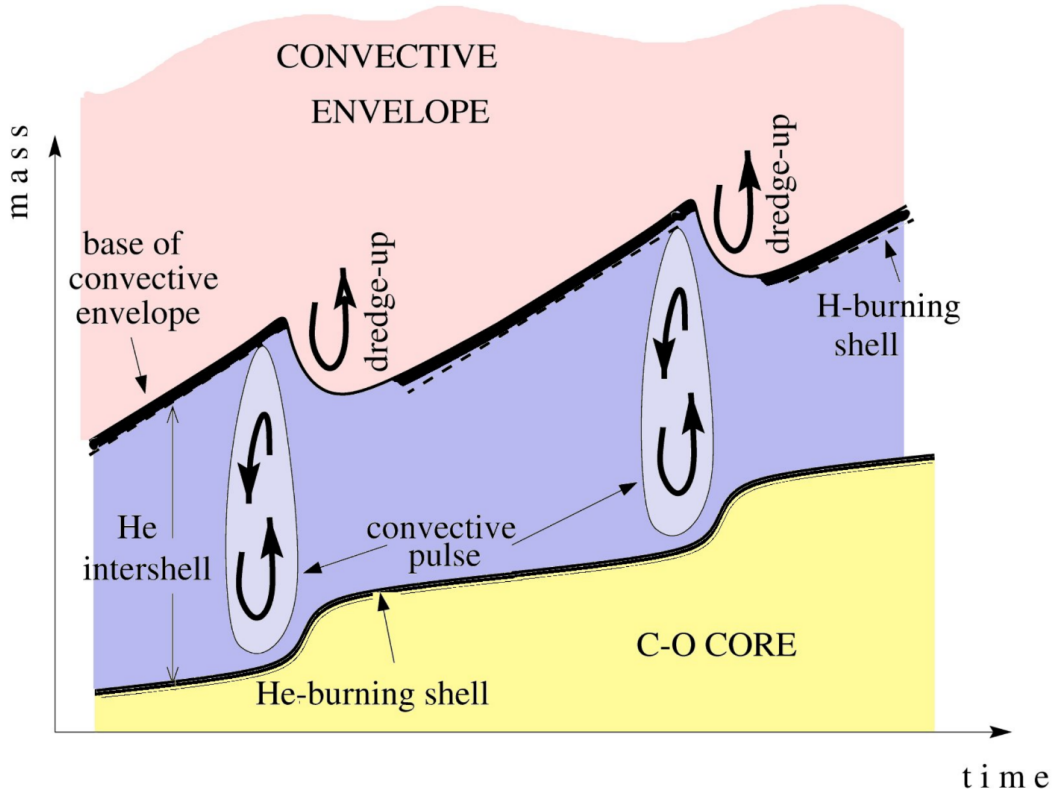

Figure 1.3: An illustration of the typical structure of AGB stars The generated elements are transported by the convective pulses across the various layers of the star, changing their abundances [1].

1.1.1 The ^{12}C and ^{13}C Ratio

As discussed earlier, the elemental abundances in the stellar atmosphere provide critical information about both stellar evolution and nucleosynthesis. The ratio of ^{12}C to ^{13}C, in particular, is a significant observable since it can be readily detected in stellar spectra [6] and is sensitive to non-standard mixing processes [7]. Specifically, the carbon isotopic ratio in Red Giant Branch

(RGB) stars can offer insights into their nucleosynthesis stage and mixing processes. For example, observations indicate that the occurrence of first dredge-up (FDU) is linked to lower atmospheric ratios [6]. However, standard stellar models do not accurately reproduce these abundances, necessitating the inclusion of extra-mixing processes to model stars ascending the Red Giant Branch [6]. Currently, thermohaline-induced mixing appears to yield the most promising results for low-mass stars, though some discrepancies remain [6]. For higher-mass stars, rotation-induced mixing is required to explain the observed abundances, which are unaffected if the star mass is too low [7]. A similar conclusion was reached in [8], which proposed a different type of mixing potentially derived from magnetic buoyancy effects within these stars, providing a good description of the observed isotopic ratios. However, intense magnetic fields deep within the stars are required, for which little evidence exists in the literature. Nevertheless, magnetic buoyancy mixing has been successfully used to describe other important variables in Asymptotic Giant Branch (AGB) stars, such as the formation of the ^{13}C pocket [9], suggesting its relevance in AGB star mixing processes. Conversely, rotation-induced mixing can also explain the ^{13}C pocket formation [10].

Other studies focused on AGB stars highlight the necessity of extra mixing processes, as evidenced by lower-than-expected ^{12}C/^{13}C ratios [11]. The ^{12}C brought to the surface during thermal pulsing and third dredge-up (TDU) events must be offset by its destruction as it traverses hydrogen-burning regions, where ^{12}C is partially converted into ^{13}C, leading to lower surface ratios. Similar conclusions are drawn from studying presolar silicon carbide (SiC) grains [12]. These grains, thought to form in the loosely bound atmospheres of AGB stars, serve as valuable tools for testing AGB star models. Recent studies have found some SiC grains with anomalies in the ^{12}C and ^{13}C isotopic ratios, which remain poorly understood due to the limited knowledge of the extra mixing processes within some AGB stars [13].

Furthermore, the ^{12}C/^{13}C ratio serves as a useful tracer for the chemical evolution of galaxies. A study found a positive gradient of the carbon isotopic ratio relative to the distance from the galactic center [14]. The ^{12}C in the interstellar medium (ISM) is believed to be produced in three scenarios: AGB stars losing mass through TDU episodes, massive stars exploding as supernovae, and white dwarfs accreting material from a companion star and subsequently exploding as supernovae [52]. In contrast, ^{13}C is primarily expelled by AGB stars through the CNO cycle. This contribution is delayed due to the longer lifetimes of low- or intermediate-mass AGB stars. Therefore, the observation of a positive gradient is a direct result of more frequent stellar cy-

cling in the galaxy's dense central regions compared to the outer regions [14]. This hypothesis aligns well with the data, suggesting that the $^{12}C/^{13}C$ ratio can be used to estimate the time and location of planetary system formation, as this ratio is fixed at their formation time.

Finally, to improve models for extra mixing in both RGB and AGB stars and to achieve a more precise description of the chemical evolution of galaxies, it is essential to have accurate reaction rates the $^{13}C(p,\gamma)^{14}N$ reaction. This is because the carbon isotopic ratio in hydrogen-burning regions is directly proportional to this quantity.

1.2 Nuclear Reactions in Stars

The reaction rate which is defined as the number of reactions per unit volume and time is a crucial parameter to comprehend star evolution and nucleosynthesis. The reaction $X(a,b)Y$ describes the following process:

$$a + X \longrightarrow Y + b \tag{1.1}$$

where $a + X$ is the entrance channel and $Y + b$ is the exit channel.

For a particular exothermic reaction, the energy released is represented by the Q-value. By taking energy conservation into account, the Q-value is represented as:

$$Q = (M_a + M_X - M_Y - M_b)c^2 \tag{1.2}$$

where M_a and M_X are mass of the particles in the entrance channel and M_Y and M_b are mass of the particles in the exit channel [3].

The reaction rate, r_{aX} , for this process is defined as follows:

$$r_{aX} = N_a \cdot N_X \cdot v \cdot \sigma(v) \tag{1.3}$$

where N_a and N_X are the number densities of particles a and X respectively, v is the relative velocity between the two entrance channel particles, and $\sigma(v)$ is the cross-section expressed as a function of v. In a good approximation, the star plasma can be modelled as an ideal gas made up of a variety of free, non-interacting particles and because of the high temperature, it can also

be considered completely ionised. The relative velocities between the plasma particles are given by Maxwell-Boltzmann distribution $\varphi(v)$:

$$\varphi(v) = 4\pi v^2 (\frac{\mu}{2\pi kT})^{\frac{3}{2}} \exp(-\frac{\mu v^2}{2kT}) \tag{1.4}$$

where μ is the reduced mass of the two particles system, k is the Boltzmann constant and T denotes the stellar temperature. Alternatively, $\varphi(v)$ can be expressed in terms of kinetic energy, E, as:

$$\varphi(E) \propto \exp(-\frac{E}{kT})E \tag{1.5}$$

Having expressed this, it is now possible to define reaction rate as the following,

$$r_{aX} = N_a \cdot N_X \cdot \int_0^\infty \varphi v \sigma(v) dv = N_a \cdot N_X \cdot < \sigma v >_{aX} \tag{1.6}$$

where $< \sigma v >_{aX}$ is the reaction rate per particle pair. By inserting the Maxwell-Boltzmann distribution, $< \sigma v >_{aX}$ is defined as:

$$< \sigma v >_{aX} = (\frac{8}{\pi\mu})\frac{1}{(kT)^{\frac{3}{2}}} \int_0^\infty \exp(-\frac{E}{kT})\sigma(E)EdE \tag{1.7}$$

The cross-section can be expressed in terms of a quantity called the astrophysical factor S-factor $S(E)$ which contains all the essential nuclear effects in the reaction. It is given by:

$$S(E) = E\sigma(E)e^{2\pi\eta} \tag{1.8}$$

where μ is the Sommerfield parameter. Numerically, we find:

$$2\pi\eta = 0.989534 Z_0 Z_1 \sqrt{\frac{1}{E}\frac{M_0 M_1}{M_0 + M_1}} \tag{1.9}$$

where the energy E is in MeV and the relative atomic masses M_i are in units of u. The latter is the variable that incorporates all the nuclear structure proprieties of a compound that is being formed and as such has a much more steady dependence on the energy, since the exponential has been factored out. This is incredibly helpful for extrapolating the cross-section at the energy ranges of interest, which are otherwise almost inaccessible for the experiments.

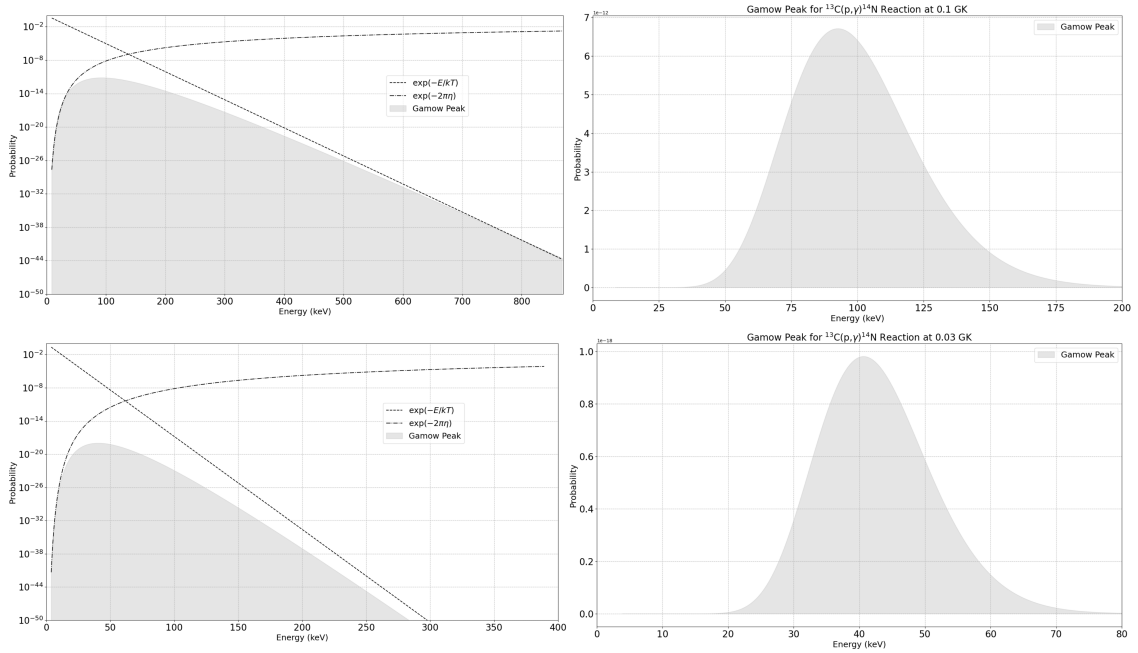

Figure 1.4: The Gamow peak (filled region) for the $^{13}C(p,\gamma)^{14}N$ reaction was computed with T = 0.1 GK (AGB star) (Top left) and was computed with T = 0.03 GK (RGB star) (Bottom left). The dashed lines on the graph represent the two contributions. The second plot shows, the Gamow peak of both stars on a linear scale.

To estimate the energy region of interest, it is possible to plug Equation 1.8 inside the reaction rate integral in Equation 1.6. The product of the cross-section and the Maxwell Boltzmann distribution gives the Gamow peak [3] which indicates the energy range at which the reaction occurs inside the stellar medium at a given temperature, being the product of the energy and reaction probabilities. An example of the Gamow peak for the $^{13}C(p,\gamma)^{14}N$ reaction is shown in Figure 1.4 for, respectively, AGB and RGB stars.

1.2.1 Proton Capture on Carbon Isotopes

The $^{13}C(p,\gamma)^{14}N$ consists of the capture of the proton by the respective carbon isotopes and the consequent production of a nitrogen isotope. The reaction is exothermic, ie. the energy is released due to the fact that the binding energies per nucleon of ^{14}N is higher than in the respective carbon nuclei [3]. The total difference in the binding energies is called the *Q*-value of the reaction and can be easily calculated from the initial and final masses of the nuclei. In this case of the $^{13}C(p,\gamma)^{14}N$, the Q-value is (7550.5636 ± 0.0003) keV [15].

The capture of the proton can occur through two different mechanisms, namely the direct capture (DC) or resonant capture. The former refers to a mechanism where a proton is captured by a nucleus without any intermediate steps: it directly merges with the nucleus, resulting in the formation of the new compound, whether in its ground state or in an excited state, and in the simultaneous emission of a γ-ray. In contrast, resonant capture involves a two-step process. First, the incoming proton forms the compound directly in its excited state, known as a resonance. This subsequently decays to its ground state by emitting γ-rays. Resonant capture is characterized by the involvement of specific energy levels in the compound nucleus, making it highly dependent on the total energy of the reactants, ie. Q-value plus the proton energy, matching the resonant energy of the nucleus.

In the reaction of interest, no resonance is present in the Gamow windows of the hydrogen-burning regions in both AGB and RGB stars. Nevertheless, two excited states are present in the ^{14}N nuclei, at approximately E_p = 551 keV, which tail can affect the cross-section even at lower energies. The level scheme of the reaction is shown in Figure1.5. In this reaction ^{13}C(p, γ)^{14}N several different excited states can be populated through the DC process and many more γ-rays are emitted, given the much complex γ-cascades. Since the γ-rays are emitted in the reaction, these can be counted and associated with the number of occurred reactions, N_r. By dividing this term by the number of incoming protons, N_p, a quantity called reaction yield, Y, is obtained which then is linked to the reaction and target proprieties, ie. cross-section, $\sigma(E)$, target thickness, ΔE, and the effective stopping power, $\varepsilon(E)$, as follows [3]:

$$\left[\frac{N_r}{N_p}\right]_{exp} = Y = \left[\int_{\Delta E} \frac{\sigma(E)}{\varepsilon(E)} dE\right]_{theo} \tag{1.10}$$

These equations make it possible to link the experimental variables to the cross-section that can be then promptly extracted by using the information provided on the target thickness. Since an integral is present on the right part of the equation, the value that is obtained is in reality the mean cross-section averaged over the energies spanned over the target. Thus, in order to correct for this issue, the effective energy, E_{eff}, that is then associated with the cross-section, is calculated as follows [3]:

$$E_{eff} = \frac{\int_{\Delta E} \sigma(E) E dE}{\int_{\Delta E} \sigma(E) dE} \tag{1.11}$$

The equations 1.10 and 1.11 are fundamental to obtain the cross-section for the reaction under study. The following review of all the literature studies for the reaction will be revised.

1.2.2 State of the Art - ^{13}C(p,γ)^{14}N

The ^{13}C(p,γ)^{14}N reaction has been the subject of many experiments over the years. Most of these experiments have concentrated on measuring the cross section for the capture to the ground state. However, only one study measured the cross-section for all the transitions. Figure 1.6 presents the literature data for the cross-section in the form of the astrophysical *S*-factor, specifically for the ground state capture. Brief descriptions of each study are provided below:

Hester and Lamb (1961) [16] In this measurement, graphite targets with a 1.1% abundance of ^{13}C were used. A NaI crystal was employed to count the emitted γ-rays, and the efficiency was determined by extrapolating the integral bias curve. The accelerator voltage had a stated precision of 1%. The cross-section was obtained from the observed yields, assuming an infinitely thick target. The obtained values agree with those from the Woodbury and Fowler (1952) measurement.

Vogl PhD. Thesis (1964) [17] The ^{13}C(p,γ)^{14}N measurements were conducted in the same manner as the ^{12}C(p, γ)^{13}N measurements. Only the cross-section values for the transition to the ground state are reported. Generally, the results show good agreement with previous studies. However, there is a slight discrepancy compared to the results of Hester and Lamb (1961).

J.D.King et al.(1994) [18] In this study, six different transitions in the ^{13}C(p,γ)^{14}N reactions were investigated over a beam energy range of 120 keV to 950 keV. Two different accelerator setups were used for measurements in the energy ranges E_p=120–325 keV and E_p=120–325 keV. Targets were prepared by evaporating carbon powder, enriched up to 99% in ^{13}C, onto tantalum backings, and characterized using the 448 keV narrow resonance. As an additional cross-check, the shape of the primary γ-ray was used to estimate target thickness. γ-rays were observed with both Ge(Li) and Ge detectors, calibrated for efficiency with calibration sources and proton-induced reactions. Detectors were positioned at 0°, 45°, 90°, and 135°, allowing for the study of the angular distribution of several primary transitions. Absolute cross sections were obtained relative to the ^{14}N(p, γ)^{15}O and ^{19}F(p, $\alpha\gamma$)^{16}O resonances. The obtained energy of the broad resonance at 0.55 MeV is shifted by approximately 5 keV compared to Vogl's PhD

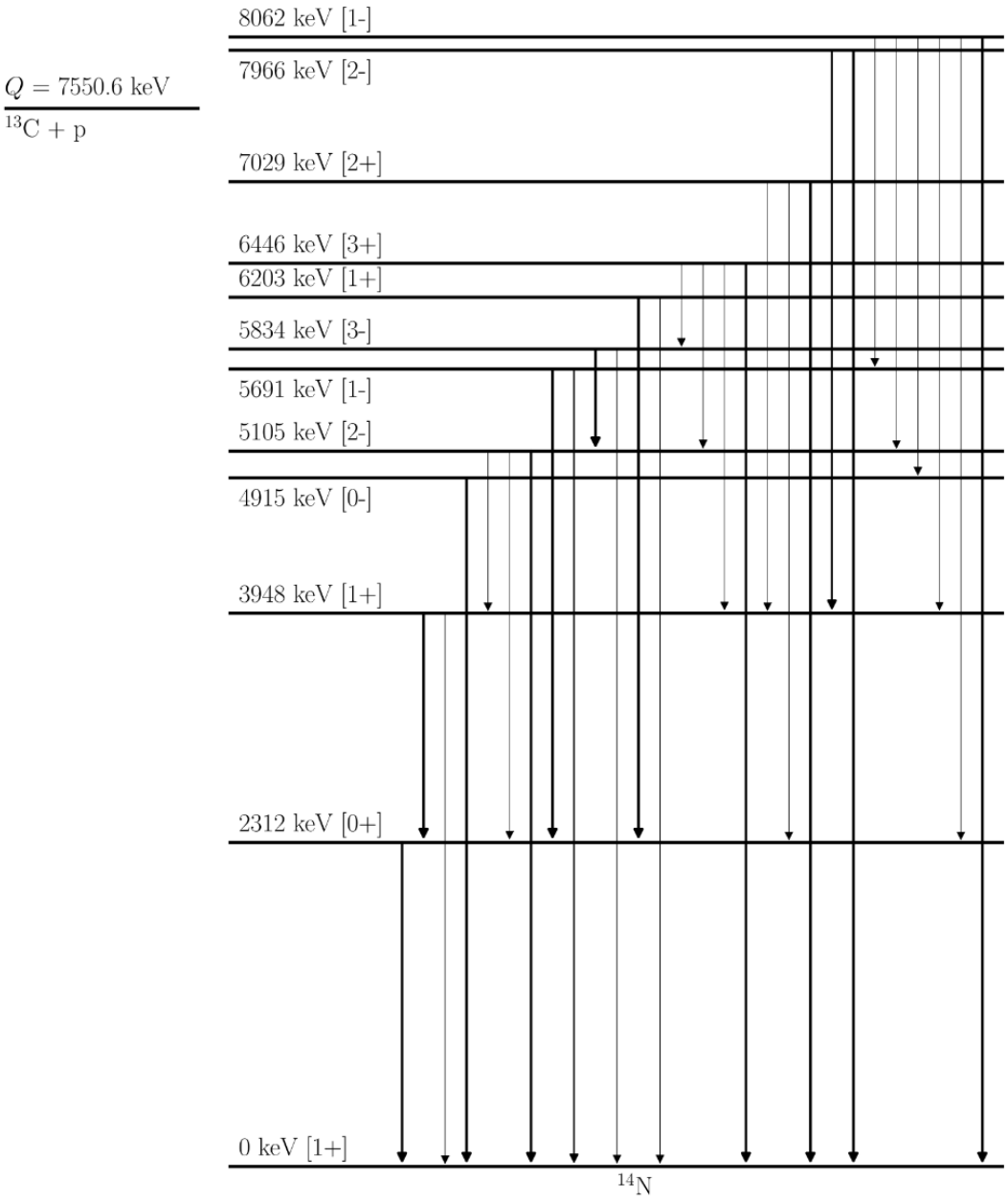

Figure 1.5: The level scheme for the ^{13}C(p, γ)^{14}N reaction. The first 6 lowest levels are mainly populated by the direct capture process, which then decays by following their γ-ray cascade.

thesis (1963). A systematic uncertainty of 11.7% is reported for the absolute normalization. Finally, the extrapolations to stellar energies were obtained, and the reaction rate was calculated.

Zeps et al. (1995) [19] This study focuses on the nuclear theory describing the mixing within nitrogen nuclei. However, it also examines many resonances in the energy range between 500 keV and 2000 keV, reporting new $\omega\gamma$ values for high-lying resonances. No information is provided on target production, which was characterized using the narrow resonance at 1.75 MeV. Both NaI and Ge(Li) detectors were used to count the emitted γ-rays. Regarding cross-section data, only non-normalized values are available. The reported energy for the 0.55 MeV resonance suggests a possible 5 keV discrepancy with the results of King et al. (1994).

Genard et al. (2010) [20] Unlike other studies, this reaction was performed using inverse kinematics. A ^{13}C beam was directed at a ^{1}H target implanted in a silicon backing. An HPGe detector was used to detect the γ-rays. The ^{15}N(p, $\alpha\gamma$)^{12}C reaction was employed to characterize the target. The cross-section was measured in the energy range of E_p=225−561 keV, specifically for the transition to the ground state. The result for the $\omega\gamma$ of the 551 keV resonance is approximately 30% lower than the value reported by King et al. (1994). However, this work was never published and exists only as a conference proceeding.

J. Skowronski et al. (2023) [21] In this recent study five different transitions in the ^{13}C(p,γ)^{14}N were investigated over a beam energy of 60 keV to 370 keV in 10 keV steps. The 400 kV LUNA accelerator provided a proton beam (up to 400 μA) in the energy range E_{cm}: 60−370 keV. target used ^{12}C and 99% enriched ^{13}C powders evaporated onto chemically cleaned Ta backings, which were produced and characterized at ATOMKI. The Statistical uncertainties are of the order of 1% for most of the data points (10% below 90 keV); systematic uncertainties are of the order of 7%–8%. They found that the S-factors is are systematically lower than most of those in the literature and dominate R-matrix extrapolations at the lowest energies.

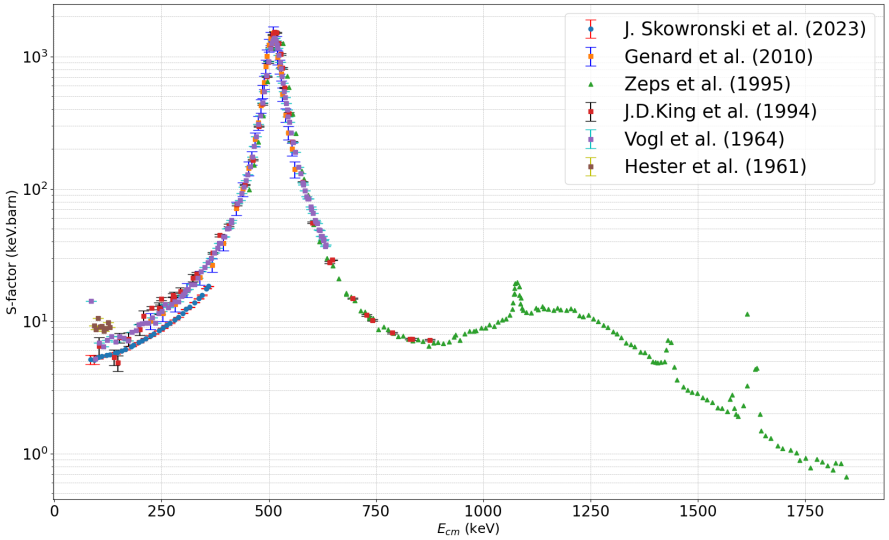

Figure 1.6: The literature S-factor values for the $^{13}C(p,\gamma)^{14}N$ reaction. Only the transition to the ground state is shown since it is the most studied one. The Zeps data were arbitrarily re-normalized to make them comparable with the other datasets.

2

Experimental Setup

The study of $^{13}C(p,\gamma)^{14}N$ reaction was performed using a 5 MV pelletron accelerator at Felsenkeller shallow Underground facility, Dresden (Germany). The beam transmission is optimised using several focusing and collimating elements installed on the beamline. The scattering chamber and the target holder were adapted to minimise the target degradation and precisely measure the beam current. A High Purity Germanium (HPGe) cluster detector, placed in close geometry is used to detect the γ-rays from the $^{13}C(p,\gamma)^{14}N$ reaction. The description of the apparatus used can be divided into two parts: Gamma Background and then the Experimental Setup allowing the detection of the reaction products.

2.1 Gamma Background

In charged-particle-induced reactions, the cross-section $\sigma(E)$ decreases exponentially at energies of astrophysical interest, which are below the Coulomb barrier. Studying these reactions at such low energies is challenging due to the background radiation that competes with the reaction signal. A significant source of background radiation is caused by cosmic rays. These cosmic rays, mainly composed of high-energy protons and alpha particles, produce muons when passing through the Earth's atmosphere. Muons, being highly penetrating, can interact with other particles and nuclei to produce neutrons and gamma rays, which interfere with the detection of gamma-ray signals from the actual nuclear reaction.

At the Felsenkeller facility, the cosmic ray background is reduced by 99% because the experiments are conducted under 45 meters of rock, providing natural shielding. Another source of background radiation comes from the radionuclides in the rocks and materials surrounding and inside the laboratory.

Several experiments using HPGe detectors have measured the background γ radiation in the underground Felsenkeller facility and compared it with values obtained at the Earth's surface. Figure 2.1 shows the γ spectra recorded by an HPGe detector, HZDR-2 (60% HPGe), placed at the Earth's surface and in two different underground locations: tunnel VIII and tunnel IV of the Felsenkeller facility. It is evident from the figure that for gamma energy $E_\gamma < 3$ MeV, the background radiation is dominated by the radionuclides ^{40}K, ^{238}U, and ^{232}Th present in the rock. This contribution can be reduced by adding passive or active shielding around the detector. For gamma energies above 3.5 MeV, the background radiation count is significantly suppressed compared to the counts observed in overground laboratories.

The γ-ray background radiation from cosmic rays and radionuclides present in the environment is referred to as the environmental background. Additionally, there is a significant contribution to the background from what is known as beam-induced background. In the study of the ^{13}C(p,γ)^{14}N reaction, a solid enriched up to 99% in ^{13}C target and Residual 1% impurities in ^{12}C.

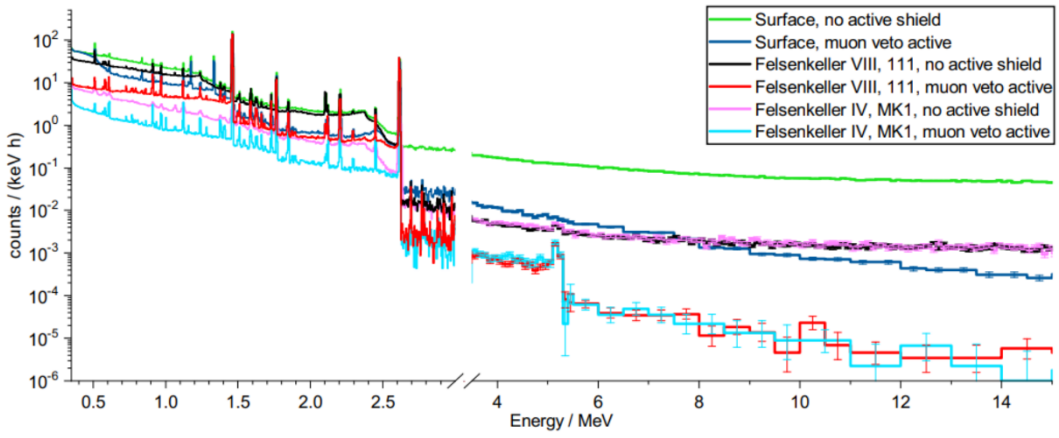

Figure 2.1: γ-ray energy spectra recorded with detector HZDR-2 (60% HPGe) at Earth's surface, underground at Felsenkeller tunnel VIII, room 111, and at Felsenkeller tunnel IV, MK1.[2]

2.2 The 5 MV pelletron accelerator

The tunnels were blasted in 1856-1859 into the hornblende monzonite rock, in order to create cool storage for the adjacent Felsenkeller brewery. From 2016-2018, TU Dresden and HZDR jointly refurbished tunnels VIII and IX for laboratory usage.

At the Felsenkeller facility, a 5 MV Pelletron tandem accelerator of type 15SDH-2 produced by National Electrostatics Corporation (NEC), USA is installed. The accelerator has been located inside the connecting tunnel between tunnels VIII and IX of the Felenskeller underground facility, see Figure 2.2.

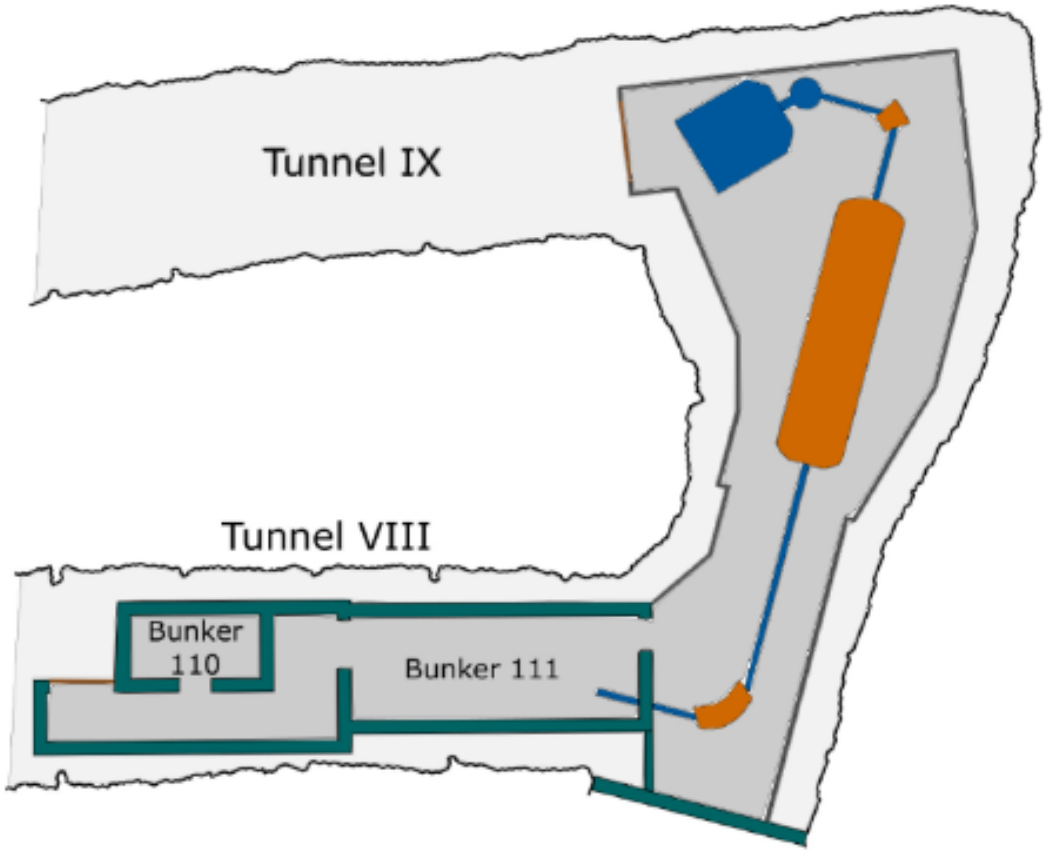

Figure 2.2: Layout of the Felsenkeller accelerator laboratory in tunnels VIII and IX [2].

The 5 MV pelletron accelerator has two different ion sources. The first one is the external caesium sputtering ion source of type 134 MC-SNICS developed by NEC and it can provide up

to 100 μA $^{12}C^{-}$ beam [2]. The second one is an internal radio frequency (RF) ion source which NEC also made. Mounted on the high-voltage terminal behind a custom-made electrostatic deflector, this ion source can work in both tandem and single-ended modes. In tandem mode, heavy mass particles like C, N, and O can be accelerated while in a single-ended mode light mass ions like H or He are provided by the 5MV Pelletron accelerator. It was found that the RF ion source can deliver up to 90 μA $^{4}He^{+}$ beam. Because of this distinctive combination, various hydrogen and helium-burning processes that occur in the stars can be investigated. For the present $^{13}C(p,\gamma)^{14}N$ experiment, the pelletron was used in single-ended mode providing $\approx$ 10 μA of H_2^+ beam. A $\approx$ 1 μA proton beam was also provided for the target characterisation and efficiency measurement.

2.2.1 The scattering chamber

The well-collimated proton H_2^+ beam reaches the target with a final diameter of 5 mm. The energy range covered by the molecular beam was 350 - 700 keV, while proton beam were used for efficiency and target monitoring aims. Both the scattering chamber and the target are insulated from the beamline, thus they act as a Faraday cup allowing the direct reading of beam current directly during each measurement. Secondary electrons are produced due to the interaction of the beam particles with the target. These electrons escape from the target and cause incorrect current readings. In order to suppress the secondary electrons, a copper tube was installed inside the chamber, at a distance of 10 mm from the target. A negative potential of 200 V was applied to the copper tube, to deflect electrons emitted from the target back onto it. The scattering chamber and the target beamline were both isolated from the copper tube. Additionally, the copper tube was used as a cold finger during the measurement to avoid carbon build-up on the target. This was achieved by keeping the copper tube in thermal contact with LN_2.

2.2.2 Targets

Target was mounted at 55° with respect to beam direction and it was water cooled in order to limit target degradation. For the present work, two targets of slightly different thicknesses were irradiated.

The targets were produced at ATOMKI Laboratories, Hungary, by evaporating enriched carbon powder consisting of 99% ^{13}C and 1% ^{12}C, 170-350 nm thick (corresponding to 14-30

keV proton energy loss at E_b = 500 keV) exploited to assess and reduce systematic uncertainties related to the target thickness and profile.

The evaporation process was carried out using an electron gun technique with a Leybold UNIVEX 350 vacuum evaporator at Atomki. The natural ^{13}C powder is placed in a copper melting pot and then heated using an electron gun. an adjustable arm used to hold the tantalum disk at 10 cm from the melting pot, and an electron gun. In order to monitor the evaporation, oscillator quartz mounted inside the vacuum chamber at 15 cm from the melting pot, which can measure the thickness of the deposition online [22]. The evaporation procedure can cause changes to the target composition, as a result, the target thickness and composition are generally determined through dedicated experiments. The method used for target characterization are detailed in later sections.

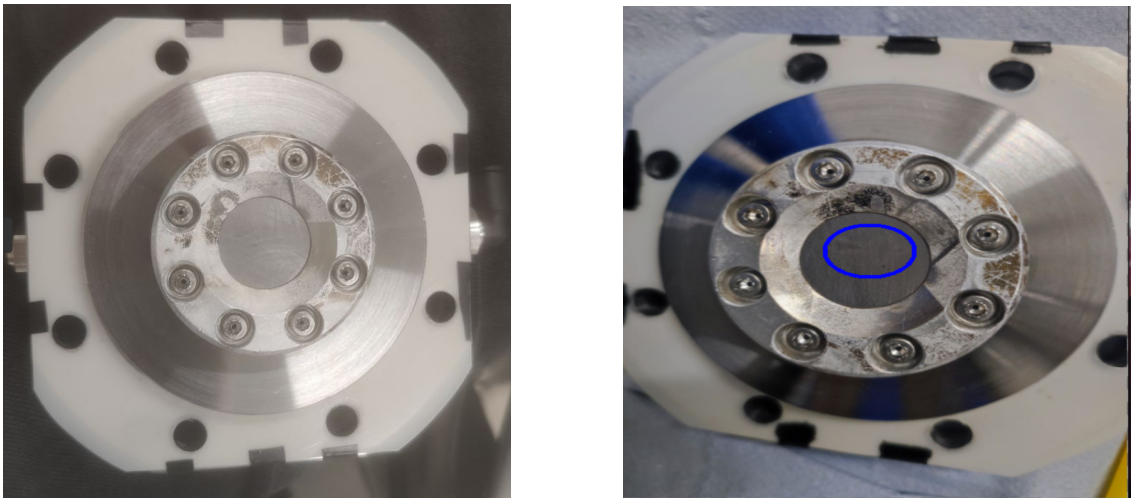

Figure 2.3: Comparison of the target before (Left) and after (Right) it got irradiated by the proton beam. Beam spot in the blue circle on the irradiated target.

2.2.3 HPGe Detectors

An HPGe detector was used to detect the γ-rays. The HPGe detectors are based on the principle of semi-conductive properties of germanium (Ge). Due to its low band gap (0.7 eV), Ge can give rise to a high number of charge carriers (electron-hole pairs) and is hence helpful in determining the intensity of the incoming photon radiation to a good extent. In addition to this, the energy resolution of the HPGe detectors is high, e.g. the energy resolution was found to be around 2 keV at gamma energy E_γ = 1.3 MeV as reported in [23]. However, due to the limited size and low atomic number of Ge, the efficiency of an HPGe detector is low for energies $E_\gamma >$ 1 MeV when compared with scintillators [23].

The solid target used in studying this reaction was surrounded in total by 5 HPGe-cluster detectors as shown in Figure 2.4, The main detector, used for the cross-section determination, is located in close geometry (3.5 cm from the target) at 55° with respect to the beam direction (RON100) and since this is the only detector that can be moved it placed at 5,10,15 and 20 cm from the target. To investigate the angular distribution, the other HPGe detectors located at different angles, ranging from 90° to 130°, namely MB1, MB2, EB17, EB18, and a single crystal detector RON100, see Table 2.1 and Figure 2.4.

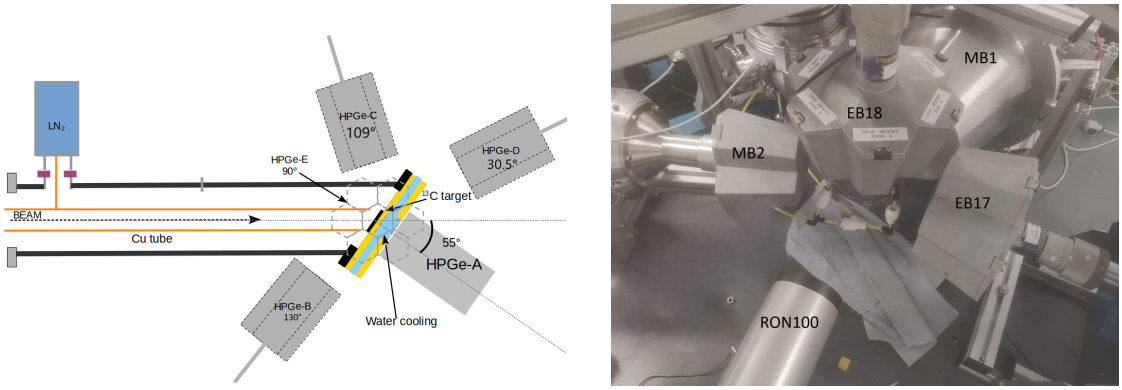

Figure 2.4: The experimental detectors scheme configuration (Left), and the experimental configuration during the measurement (Right).

Detector ID	Type	Relative Efficiency (%)	Angle (°)	Distance (cm)
RON100 (HPGe-A)	Single	100	55	3.5, 5, 10, 15, 20
MB1 (HPGe-B)	Clover - 3 crystals	3 × 60	130	18.8
MB2 (HPGe-C)	Clover - 3 crystals	3 × 60	109	11.1
EB18 (HPGe-D)	Clover - 7 crystals	7 × 60	90	12.9
EB17 (HPGe-E)	Clover - 7 crystals	7 × 60	30.5	6

Table 2.1: Details of 5 HPGe cluster detectors used in the study of $^{13}C(p,\gamma)^{14}N$ reaction.

3
Data Analysis

3.1 Gamma Spectrum

In the obtained γ-spectra at E_p = 500 keV which is shown in Figure 3.1. No other contaminants other than the nominal 1% of ^{12}C and the ^{19}F were found inside the targets after carefully inspecting all the spectra by the reaction $^{19}F(p,\alpha\gamma)^{16}O$ which has a Q_{value}= 8114 keV and has a rather high cross-section at energies close to E_p = 500 keV resonance. ^{16}O is populated in an excited state and its de-excitation produces a γ-ray of energy E_γ = 6128.63 keV. In addition to the full energy peak, the First and the second escape peaks are visible. The γ-peak at 2428 keV was identified as coming from the $^{12}C(p,\gamma)^{13}N$ reaction.

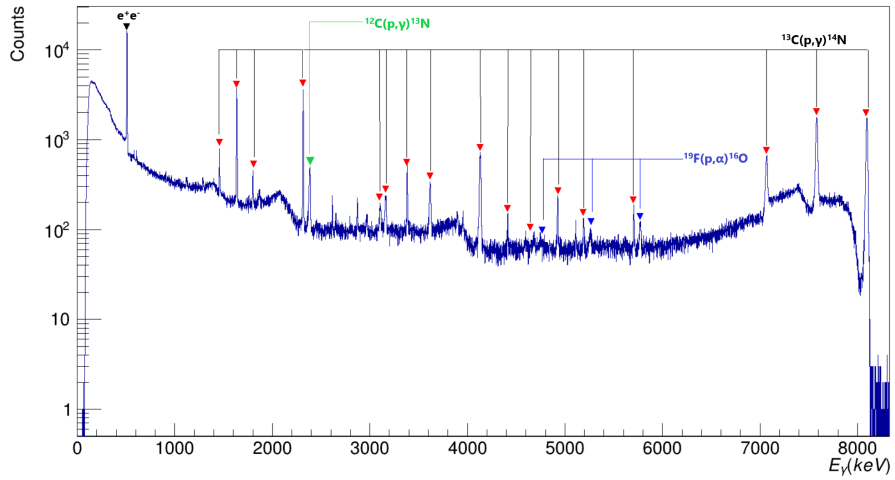

Figure 3.1: γ-spectra at E_p = 500 keV acquired at the Felsenkeller laboratory.

3.2 Yield and Cross-section

The reaction yield is the quantity measured during direct experiments and is defined as the ratio of the total number of reactions (N_R) to the total number of incident beam particles (N_b). Experimentally, the total yield is given by:

$$Y = \frac{N_R}{N_b} = \frac{N_\gamma}{N_p \eta_{pb}(E_\gamma) W(\theta) B_r} \tag{3.1}$$

where N_γ is the number of observed gamma rays, N_p is the number of incoming protons, B_r is the branching ratio of the γ-ray transition, η_{pb} is the detector efficiency and $W(\theta)$ is the angular distribution factor.

In the following equations the transformation from the laboratory to the centre of mass frame of reference in two two-body collisions is done by using the following equation:

$$E_{cm} = E_{lab} \frac{m_1}{m_0 + m_1} \tag{3.2}$$

where m_0 and m_1 are the masses of the projectile (p) and the target (^{13}C) nuclei, respectively.

The total yield Y can also be expressed in terms of the reaction cross section, σ(E), [3]:

$$Y = \frac{N_R}{N_b} = \int_{E_0-\Delta E}^{E_0} \frac{\sigma(E)}{\varepsilon_{eff}(E)} dE \tag{3.3}$$

where $\varepsilon_{eff}(E)$ represents the effective stopping power, accounting for the number of nuclei per unit area available in the target, ΔE is the total energy lost by the beam after interacting with the target, and E_0 is the beam energy.
In the case of the ^{13}C(p, γ)^{14}N reaction, it is possible to use Equation 1.8 to rewrite Equation 3.2:

$$Y = S(E_{eff}) \int_{E_0-\Delta E}^{E_0} \frac{e^{-2\pi\eta(E)}}{\varepsilon(E)E} \tag{3.4}$$

where the exponential term is the Gamow factor and η is the Sommerfield parameter. Numerically, we find:

$$2\pi\eta = 0.989534 Z_0 Z_1 \sqrt{\frac{1}{E}\frac{m_0 m_1}{m_0 + m_1}} \tag{3.5}$$

where the energy E is in MeV and the relative atomic masses m_i are in units of u.
In equation 3.3, the S-factor was assumed to be constant over the target thickness in order to calculate the integral and divide the yield by the integral to find the S-factor.
The S-factor is associated with the effective energy, E_{eff}, which is defined as the weighted average of the energy over the target thickness:

$$E_{eff} = \frac{\int_{E_0-\Delta E}^{E_0} E\sigma(E)dE}{\int_{E_0-\Delta E}^{E_0} \sigma(E)dE} \tag{3.6}$$

where here we have E in centre of mass frame of reference. By combining equations 3.1 and 3.3 we can extract the information about the reaction S-factor by experimentally obtaining the total yield measurement. To do so each component necessary for the calculation of the S-factor is explained in following sections.

3.3 Stopping power

When a charged particle travels through a particular material, it decelerates by losing some of its energy, mainly due to inelastic collisions with atomic electrons. This rate of energy loss is

known as the linear stopping power given in the following equation:

$$\varepsilon_{lin} = -\frac{dE}{dx} \tag{3.7}$$

where dE is the infinitesimal energy loss in the infinitesimal spatial distance dx. The stopping power is typically expressed as the energy loss per unit areal density, ρ (measured in units of atoms per cm^2):

$$\varepsilon(E) = -\frac{1}{N}\frac{dE}{dx} \tag{3.8}$$

where N is the number density (in units of atoms/cm^3) of the target material. A good approximation of the energy loss of the charged particle passing through matter at high energies can be approximated by using the following Bethe-Bloch formula [23]:

$$\frac{dE}{dx} = \frac{4\pi e^4 z^2}{m_e v^2} NB \tag{3.9}$$

where

$$B = Z\left[\ln(\frac{2m_e v^2}{I}) - \ln(1 - \frac{v^2}{c^2}) - \frac{v^2}{C^2}\right] \tag{3.10}$$

The previous equations describe the theoretical stopping power for a projectile of charge z with velocity v passing through a medium composed of elements with the atomic number Z, I represents the ionization potential and m_e is the mass of electron. The key points from this description are that stopping power is inversely proportional to energy (since energy is proportional to the square of velocity, $E \propto v^2$) and the energy loss is directly proportional to the charges of both the projectile and the target.

The previous discussion has been focused on targets composed of a single element. However, in nuclear physics experiments, this is often not the case. Typically, targets are made up of several different elements, and the presence of contaminants must also be considered. In such scenarios, it is necessary to calculate a quantity known as the effective stopping power, ε_{eff}[24]:

$$\varepsilon_{eff} = \varepsilon_a + \Sigma_i \frac{N_i}{N_a}\varepsilon_i \tag{3.11}$$

where N_a refers to the active nuclei and N_i refers to the inactive nuclei present in the target. The inactive nuclei are not involved in the reaction of interest but contribute to slowing down the projectile. Additionally, ε_a and ε_i represent the stopping power for active and inactive nuclei,

respectively. In the current experiment, the effective stopping power is given by:

$$\varepsilon_{eff}(^{13}C) = \varepsilon(^{13}C) + \frac{N(^{12}C)}{N(^{13}C)}\varepsilon(^{12}C) \tag{3.12}$$

In this context, ^{13}C and ^{12}C are the active and inactive nuclei present in the target, respectively (the percentage of ^{12}C is detailed in the target composition). Since the stopping power of both carbon isotopes is identical, equation 3.12 can be simplified as follows:

$$\varepsilon_{eff}(^{13}C) = \frac{N(C)}{N(^{13}C)}\varepsilon(C) \tag{3.13}$$

A computer code software called SRIM [25] is highly useful for calculating the stopping power of projectiles in various target-projectile systems at different incoming projectile energies. However, SRIM does not provide stopping power values for every possible energy level, therefore linear interpolation used to determine the stopping power at specific energies. For the ^{13}C(p,γ)^{14}N reaction, the stopping power for ^{13}C nuclei as a function of proton energy is shown in the following Figure:

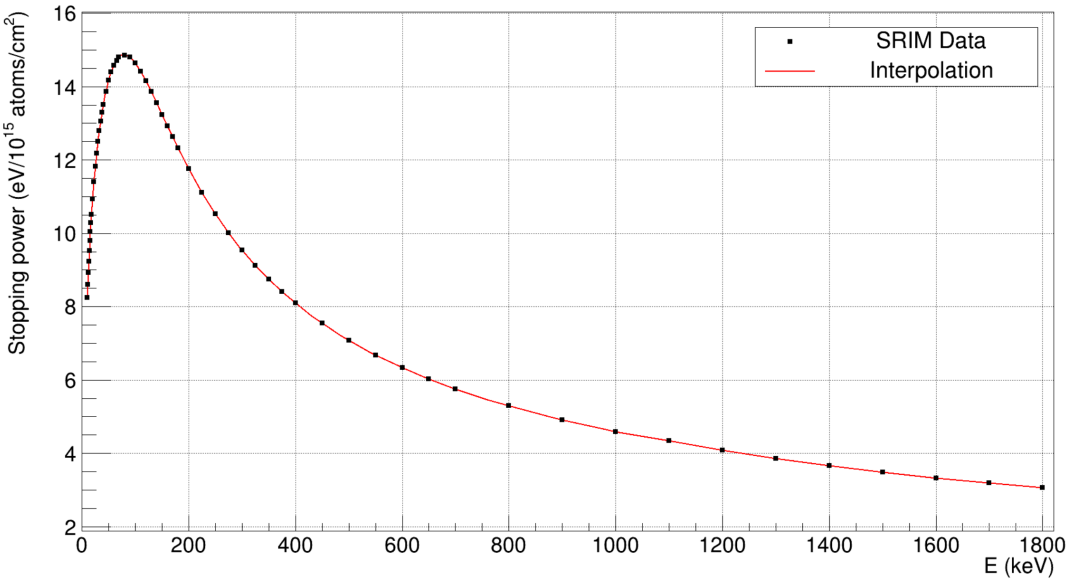

Figure 3.2: SRIM stopping power for protons inside the carbon target.

3.4 Efficiency

The efficiency calibration for the experimental setup was performed using point-like calibration sources, ^{137} Cs, ^{60} Co and ^{88}Y, the γ-rays from the well-known ^{27}Al(p,γ)^{28}Si resonance at E_p = 991 keV [26] and ^{14}N(p,γ)^{15}O resonance at E_p = 278 keV [27].

For γ-ray energies below 2000 keV, the efficiency calibration was established using the calibration sources, ^{137}Cs, ^{60}Co and ^{88}Y. The ^{137}Cs nuclei decay by emitting a single γ-ray of 662 keV. In contrast, ^{60}Co nuclei decay with a 99% probability to a 2507 keV level of ^{60}Ni via $\beta-$ decay, followed by the emission of two distinct γ-rays in sequence: the primary γ-ray at 1173 keV and the secondary γ-ray at 1332 keV. Additionally, ^{88}Y decays via $\beta+$ decay and emits γ-rays at 898 keV and 1836 keV. All sources were positioned on the target holder same as the targets.

The absolute full-energy peak efficiency is defined as the ratio of the measured peak area to the total number of γ-rays emitted by the radioactive nuclide over the entire solid angle. It can be calculated using the following equation:

$$\eta_{pb} = \frac{N_{counts}}{A\Delta t B_r} \tag{3.14}$$

where N_{counts} is the number of counts inside the γ-peak of interest, Δt is the measuring time of the experiment, B_r is the branching ratio of the emitted γ-ray, and A the activity of the source at the measurement time.

The resultant efficiencies from calibration sources, ^{27}Al(p,γ)^{28}Si reaction and ^{14}N(p,γ)^{15}O reaction taking into account two different distances for the RON100 detector can be seen Figure 3.3. The efficiency curve is fitted using the empirical formula[23]:

$$\ln(\eta_{pb}) = a + b\ln(E_\gamma) + c(\ln(E_\gamma))^2 \tag{3.15}$$

where Eγ is the γ-ray energy and a, b and c are free parameters. The efficiency curve is plotted in Figure 3.3 and the fit parameters are shown in Table 3.1.

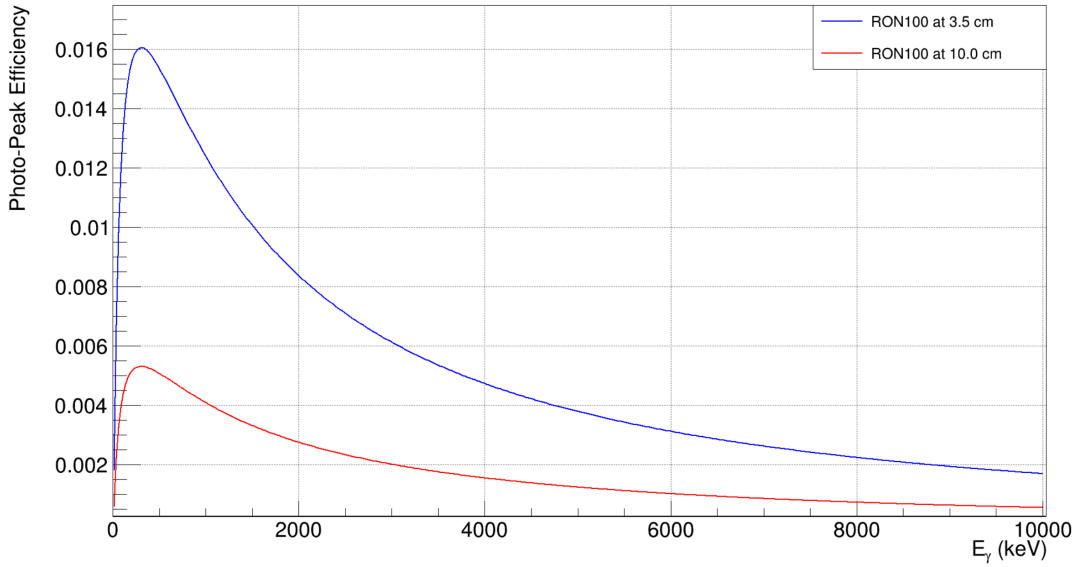

Figure 3.3: Photo-Peak Efficiency obtained with two distances of RON100 at 3.5 cm (close geometry) (Blue) and 10 cm (Red).

a	b	c
-0.2346(3)	-0.4411(7)	-0.1855(2)

Table 3.1: Efficiency curve parameters obtained by the fit.

Using the efficiency curve, we can determine the efficiency of Eγ from the ^{13}C(p, γ)^{14}N reaction.

3.5 Target Characterization

To calculate the ^{13}C(p,γ)^{14}N S-factor, the target thickness (ΔE) and target composition are needed for the effective stopping power evaluation, as referenced in equation 3.3. The target composition consists of evaporated enriched carbon targets with 99% ^{13}C and 1% ^{12}C were used. To characterize and monitor the target thickness, a scan of the ^{13} C (p, γ) ^{14} N resonance at 1749 keV was performed. By increasing E$_p$ by a few keV in each run, starting from 1748 keV, we can match the resonance energy at different layers within the target as the proton beam loses energy. A γ-ray spectrum was obtained for each measurement of the resonance scan.

The target profile of 13C_02_01 and 13C_02_02 targets obtained from multiple resonance scans can be seen in Figure 3.4 and Figure 3.5, respectively, its good to mention here that some of the resonance scans not used because the data obtained has the same energy value, The experimental yield curve from the resonance scan can be fit using two Fermi functions as follows [22]:

$$Y = Y_{max}\left[\exp(\frac{E_p - E_0}{\Gamma_1}) + 1\right]^{-1}\left[\exp(\frac{E_0 - E_p - \Delta E}{\Gamma_2}) + 1\right]^{-1} \tag{3.16}$$

where E_0 is the incident beam energy, ΔE is the target thickness, and Γ_1 and Γ_2 are two parameters accounting, respectively, for the slopes of the falling and leading edges of the target profile.

The target thickness ΔE obtained from the fit can be seen in Figure 3.6 for both targets which shows that no target degradation along with the Accumulative charge Q_{acc}, in the following table average results of the fit:

Target	ΔE (keV)
13C_02_01	5.6475 ± 0.1953
13C_02_02	4.498 ± 0.492

Table 3.2: The target thicknesses obtained from Scans fit.

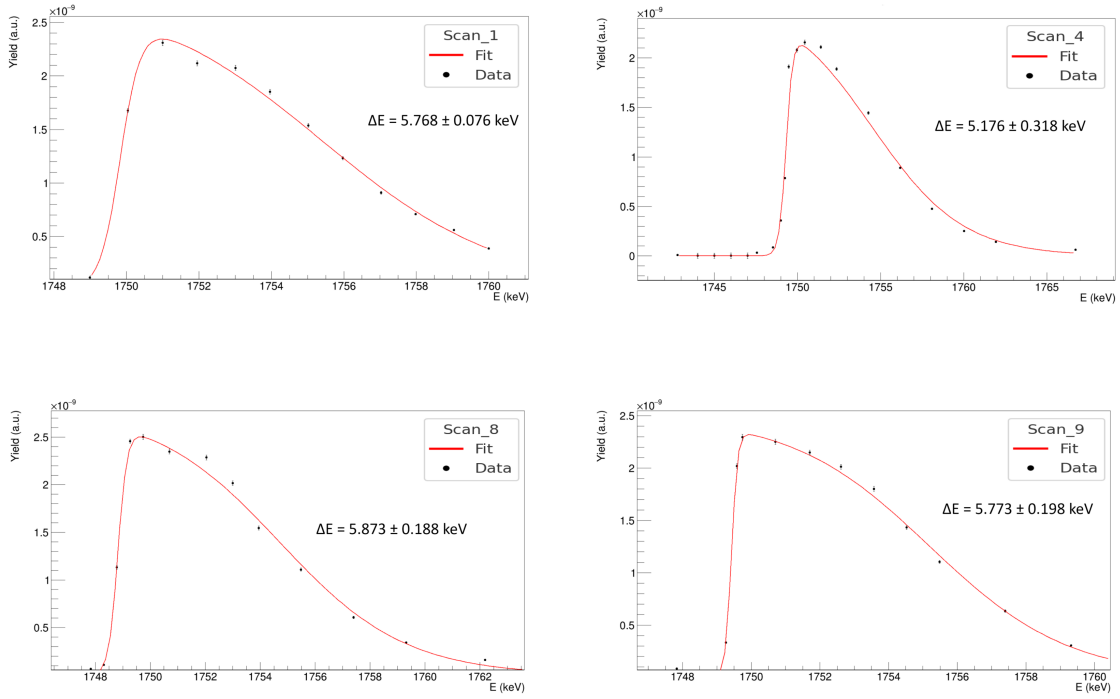

Figure 3.4: Fitted Resonance Scan perfomed using 13C_02_01 target.

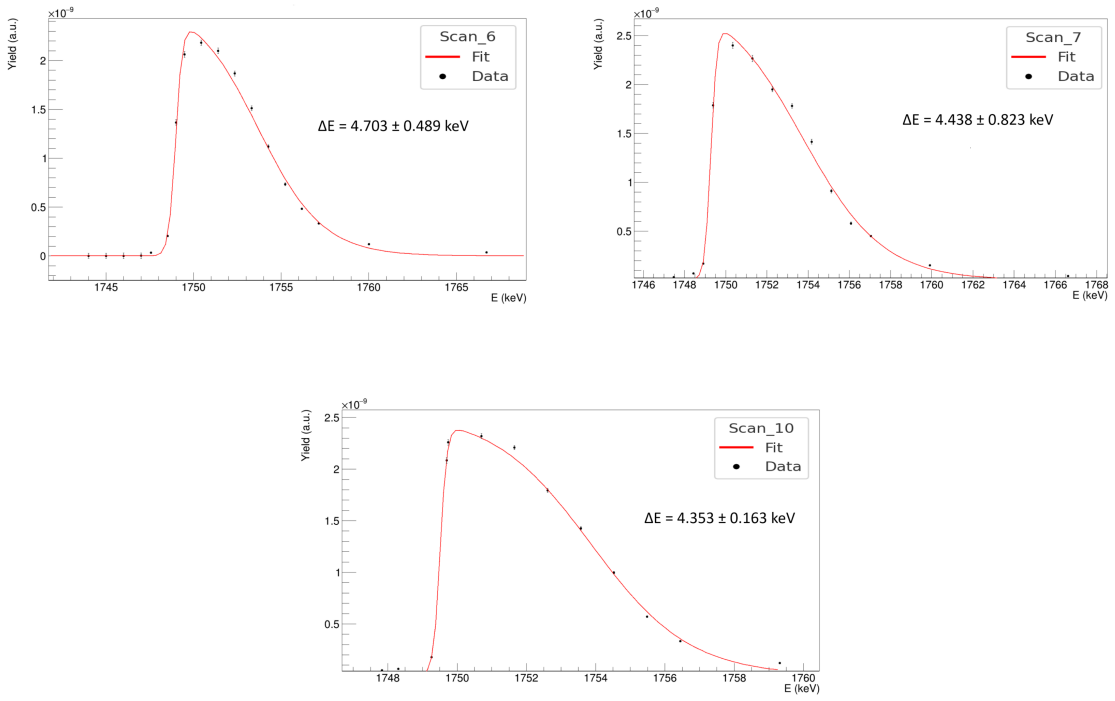

Figure 3.5: Fitted Resonance Scan perfomed using 13C_02_02 target.

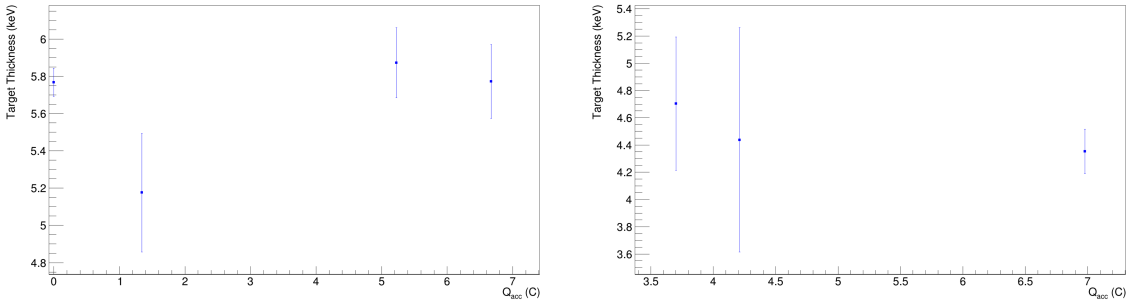

Figure 3.6: Target Thickness obtained from fit resonance Scans performed on Target 13C_02_01 (Left) and 13C_02_02 (Right).

3.6 Yield Analysis of $^{13}C(p,\gamma)^{14}N$

The region of interest (ROI) for the peak, which highly depends on the target thickness, was visually selected. An evaluation of the tail's impact was conducted by calculating the integral for the tail and the peak, confirming that the tail contributes only 1% to the net counts, as can be seen in Figure3.7.

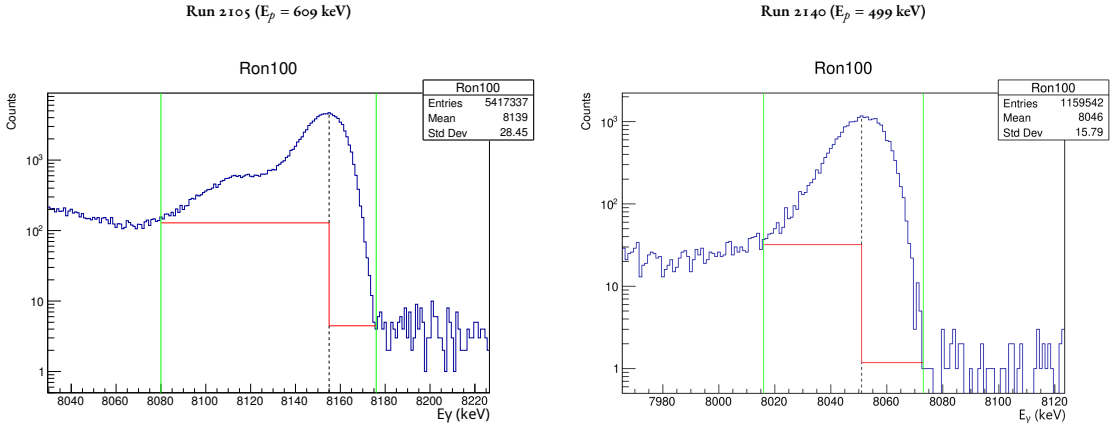

Figure 3.7: Two peaks for the 13C_02_01 target. Both are on a logarithmic scale; the one on the left shows the contribution of the tail for the low-energy side. ROI is between the green lines, and the red line is the background suppression.

The net counts are calculated by subtracting the background counts (N_B) from the total number of counts (N_T). The background counts are determined by the area under the γ-peak, using a step-like function that fits the background on both the left and right sides of the ROI.

$$N_{counts} = N_T - N_B \tag{3.17}$$

$$\sigma^2_{counts} = \sigma^2_T + \sigma^2_B \tag{3.18}$$

where σ_{counts} is the calculated statistical error, and σ_T and σ_B are the errors of the peak counts and background counts, respectively, both calculated assuming a Poisson distribution.

To calculate the reaction yield, the number of incoming protons (N_p) was determined using the following formula:

$$N_p = \frac{2Q_{run}}{q_e} \tag{3.19}$$

where Q_{run} is the accumulated charge during each experimental run, and q_e is the elementary charge.
The yields are calculated using the equation 3.1. The yield for both the targets (13C_02_01 and 13C_02_02) for all the energy runs are shown in logarithmic scale in the Figures 3.8-3.13.

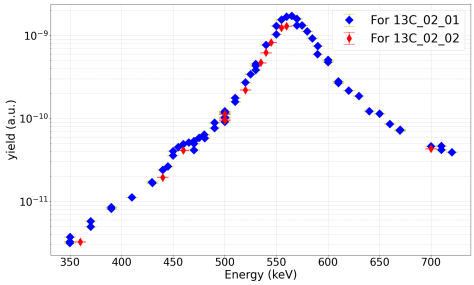

Figure 3.8: The Yield as a function of beam energy in lab frame for both targets of DC → gs.

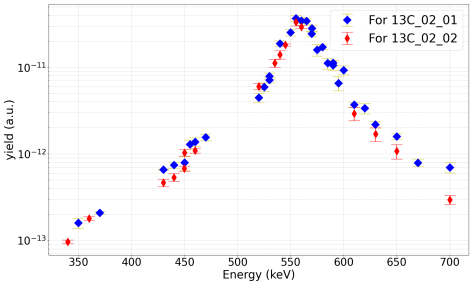

Figure 3.9: The Yield as a function of beam energy in lab frame for both targets of DC → 2312 keV.

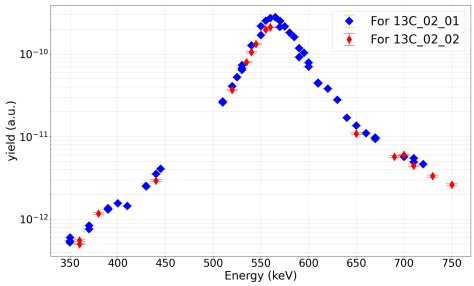

Figure 3.10: The Yield as a function of beam energy in lab frame for both targets of DC → 3948 keV.

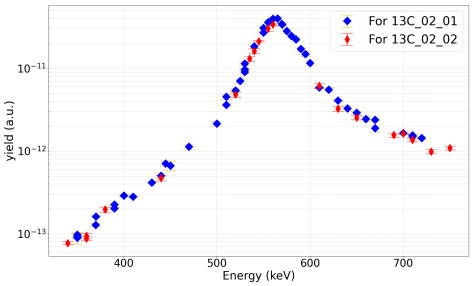

Figure 3.11: The Yield as a function of beam energy in lab frame for both targets of DC → 4915 keV.

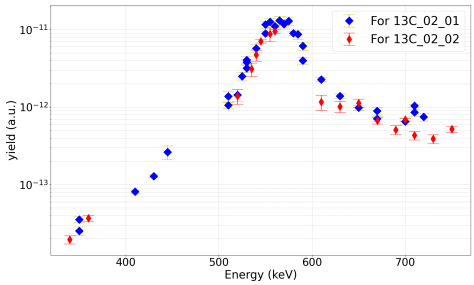

Figure 3.12: The Yield as a function of beam energy in lab frame for both targets of DC → 5105 keV.

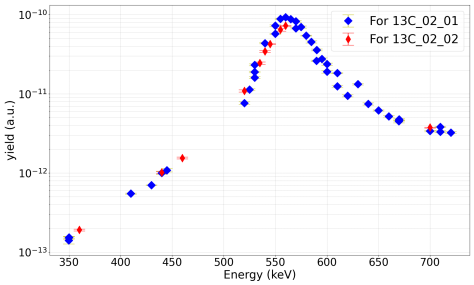

Figure 3.13: The Yield as a function of beam energy in lab frame for both targets of DC → 5691 keV.

The yields of the 13C_02_01 target are higher than those of the 13C_02_02 target, which may be attributed to the difference in their thicknesses. The 13C_02_01 target is slightly

thicker, as discussed in Section 3.5.

3.7 S-factor Calculation

The S-factor was calculated using Equation 3.4 for the proton beam energy range E_p = 350 - 700 keV. The effective stopping power, ε_{eff}, was calculated using equation 3.6. The ΔE for the integration range in the S-factor calculation was determined by taking the FWHM of the target profile, Y(E) mentioned in section 3.5. The preliminary S-factors for both targets are shown in logarithmic scale in Figure 3.14-3.19 and compared with literature data.

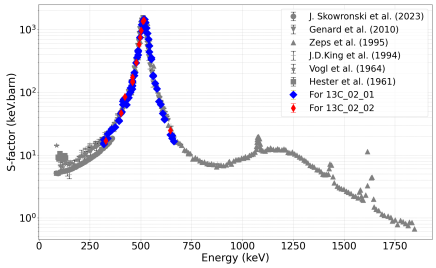

Figure 3.14: The preliminary S-factor as a function of beam energy in centre of mass frame for both targets of DC → gs.

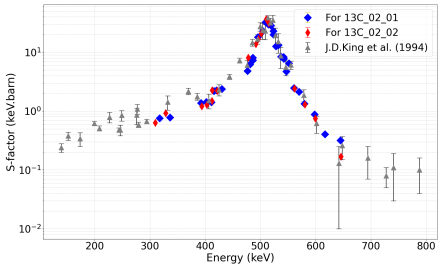

Figure 3.15: The preliminary S-factor as a function of beam energy in centre of mass frame for both targets of DC → 2312 keV.

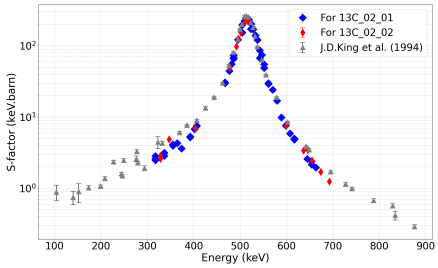

Figure 3.16: The preliminary S-factor as a function of beam energy in centre of mass frame for both targets of DC → 3948 keV.

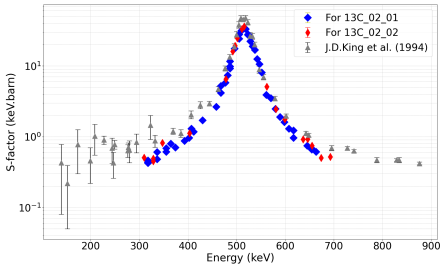

Figure 3.17: The preliminary S-factor as a function of beam energy in centre of mass frame for both targets of DC → 4915 keV.

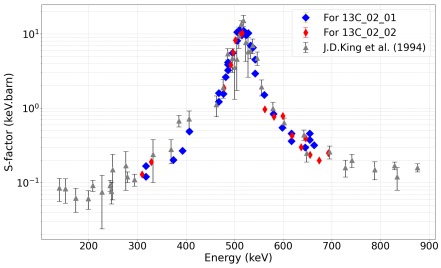

Figure 3.18: The preliminary S-factor as a function of beam energy in centre of mass frame for both targets of DC → 5105 keV.

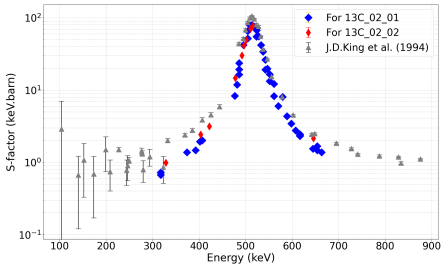

Figure 3.19: The preliminary S-factor as a function of beam energy in centre of mass frame for both targets of DC → 5691 keV.

The uncertainty in the S-factor only statistical contribution, it includes counting statistics and the uncertainty in the efficiency calculation. The systematic uncertainty of S(E) amounts to 8.5% including the contributions from detection efficiency (6.5%), stopping power (3.5%), target profile (3%), and charge collection (3%). The obtained values of the S-factor show good agreement with those reported earlier in the literature. In particular, some of the values obtained in this study agree within 8% in comparison with J.D.King et al. [18] for the transitions to gs, 2312 keV, 3948 keV and 5105 keV, There is a small discrepancy for the low energy part and at E_p = 500 keV for the transitions to 4915 keV and 5691 keV, which corresponds to the resonance peak. The reason for this discrepancy needs to be looked into with further investigation to obtain an accurate value for the resonance peak.

4

Conclusion

The $^{13}C(p,\gamma)^{14}N$ reaction is essential in the CNO cycle, influencing carbon and nitrogen isotope ratios within stars. This reaction becomes particularly significant during dredge-up episodes in the Red Giant Branch (RGB) and Asymptotic Giant Branch (AGB) phases, where deep stellar material is mixed into the outer layers. Accurate modelling of these mixing processes requires precise knowledge of the $^{13}C(p,\gamma)^{14}N$ reaction rate, as it directly affects the production of ^{14}N, which is crucial for understanding stellar evolution, surface composition changes, and the enrichment of the interstellar medium.

This thesis has reported on the experimental study to measure the S-factor of the $^{13}C(p,\gamma)^{14}N$ reaction in the energy range of 350 - 700 keV using five HPGe cluster detectors. The experiment was performed at the Felsenkeller underground facility in Dresden (Germany) using evaporated enriched carbon targets (99% ^{13}C and 1% ^{12}C). Being underground significantly reduces the environmental background, allowing for highly sensitive measurements. The efficiency of the detector was obtained using the ^{137}Cs, ^{60}Co and ^{88}Y sources, and the ^{27} Al(p,γ)^{28} Si resonance at E_p = 991 keV and $^{14}N(p,\gamma)^{15}O$ resonance at E_p = 278 keV. Scans of the 1749 keV resonance were performed to monitor and characterise the targets. Finally, the S-factor was obtained in the range 350 - 700 keV.

The performed analysis is an initial attempt for the derivation of the $^{13}C(p,\gamma)^{14}N$ S-factor. Further work is necessary to improve the results and investigate the discrepancy between the obtained S-factors and the literature data.

References

[1] D. Vescovi, "Nucleosynthesis of light and heavy elements across the Galaxy," Ph.D. dissertation, GSSI, Feb. 2021.

[2] Szücs, Tamás, Bemmerer, Daniel, Degering, Detlev, Domula, Alexander, Grieger, Marcel, Ludwig, Felix, Schmidt, Konrad, Steckling, Julia, Turkat, Steffen, and Zuber, Kai, "Background in γ-ray detectors and carbon beam tests in the felsenkeller shallow-underground accelerator laboratory," *Eur. Phys. J. A*, vol. 55, no. 10, p. 174, 2019. [Online]. Available: https://doi.org/10.1140/epja/i2019-12865-4

[3] C. Iliadis, *Nuclear Physics of Stars*, ser. Physics textbook. Wiley, 2015. [Online]. Available: https://books.google.it/books?id=iUCkBgAAQBAJ

[4] F. Herwig, "Evolution of asymptotic giant branch stars," *Annual Review of Astronomy and Astrophysics*, vol. 43, no. Volume 43, 2005, pp. 435–479, 2005. [Online]. Available: https://www.annualreviews.org/content/journals/10.1146/annurev.astro.43.072103.150600

[5] Uttenthaler, S., McDonald, I., Bernhard, K., Cristallo, S., and Gobrecht, D., "Interplay between pulsation, mass loss, and third dredge-up: More about miras with and without technetium□," *AA*, vol. 622, p. A120, 2019. [Online]. Available: https://doi.org/10.1051/0004-6361/201833794

[6] L. Szigeti, S. Mészáros, V. V. Smith, K. Cunha, N. Lagarde, C. Charbonnel, D. A. García-Hernández, M. Shetrone, M. Pinsonneault, C. Allende Prieto, J. G. Fernández-Trincado, J. Kovács, and S. Villanova, "12C/13C isotopic ratios in red-giant stars of the open cluster NGC 6791," *Monthly Notices of the Royal Astronomical Society*, vol. 474, no. 4, pp. 4810–4817, 11 2017. [Online]. Available: https://doi.org/10.1093/mnras/stx3027

[7] Charbonnel, C. and Lagarde, N., "Thermohaline instability and rotation-induced mixing - i. low- and intermediate-mass solar metallicity stars up to the end of the agb,"

AA, vol. 522, p. A10, 2010. [Online]. Available: https://doi.org/10.1051/0004-6361/201014432

[8] M. Busso, G. J. Wasserburg, K. M. Nollett, and A. Calandra, "Can Extra Mixing in RGB and AGB Stars Be Attributed to Magnetic Mechanisms?" , vol. 671, no. 1, pp. 802–810, Dec. 2007.

[9] D. Vescovi, S. Cristallo, M. Busso, and N. Liu, "Magnetic-buoyancy-induced mixing in agb stars: Presolar sic grains," *The Astrophysical Journal Letters*, vol. 897, no. 2, p. L25, jul 2020. [Online]. Available: https://dx.doi.org/10.3847/2041-8213/ab9fa1

[10] N. Langer, A. Heger, S. Wellstein, and F. Herwig, "Mixing and nucleosynthesis in rotating tp-agb stars," 1999.

[11] S. Palmerini, M. L. Cognata, S. Cristallo, and M. Busso, "Deep mixing in evolved stars. i. the effect of reaction rate revisions from c to al," *The Astrophysical Journal*, vol. 729, no. 1, p. 3, feb 2011. [Online]. Available: https://dx.doi.org/10.1088/0004-637X/729/1/3

[12] R. P. Hedrosa, C. Abia, M. Busso, S. Cristallo, I. Domínguez, S. Palmerini, B. Plez, and O. Straniero, "Nitrogen isotopes in asymptotic giant branch carbon stars and presolar sic grains: A challenge for stellar nucleosynthesis," *The Astrophysical Journal Letters*, vol. 768, no. 1, p. L11, apr 2013. [Online]. Available: https://dx.doi.org/10.1088/2041-8205/768/1/L11

[13] N. Liu, J. Barosch, L. R. Nittler, C. M. O. Alexander, J. Wang, S. Cristallo, M. Busso, and S. Palmerini, "New multielement isotopic compositions of presolar sic grains: Implications for their stellar origins," *The Astrophysical Journal Letters*, vol. 920, no. 1, p. L26, oct 2021. [Online]. Available: https://dx.doi.org/10.3847/2041-8213/ac260b

[14] S. N. Milam, C. Savage, M. A. Brewster, L. M. Ziurys, and S. Wyckoff, "The $^{12}C/^{13}C$ Isotope Gradient Derived from Millimeter Transitions of CN: The Case for Galactic Chemical Evolution," , vol. 634, no. 2, pp. 1126–1132, Dec. 2005.

[15] M. Chadwick, M. Herman, P. Obložinský, M. Dunn, Y. Danon, A. Kahler, D. Smith, B. Pritychenko, G. Arbanas, R. Arcilla, R. Brewer, D. Brown, R. Capote, A. Carlson, Y. Cho, H. Derrien, K. Guber, G. Hale, S. Hoblit, S. Holloway, T. Johnson, T. Kawano, B. Kiedrowski, H. Kim, S. Kunieda, N. Larson, L. Leal,

J. Lestone, R. Little, E. McCutchan, R. MacFarlane, M. MacInnes, C. Mattoon, R. McKnight, S. Mughabghab, G. Nobre, G. Palmiotti, A. Palumbo, M. Pigni, V. Pronyaev, R. Sayer, A. Sonzogni, N. Summers, P. Talou, I. Thompson, A. Trkov, R. Vogt, S. van der Marck, A. Wallner, M. White, D. Wiarda, and P. Young, "Endf/b-vii.1 nuclear data for science and technology: Cross sections, covariances, fission product yields and decay data," *Nuclear Data Sheets*, vol. 112, no. 12, pp. 2887–2996, 2011, special Issue on ENDF/B-VII.1 Library. [Online]. Available: https://www.sciencedirect.com/science/article/pii/S009037521100113X

[16] R. E. Hester and W. A. S. Lamb, "Radiative capture of protons in c^{13}," *Phys. Rev.*, vol. 121, pp. 584–586, Jan 1961. [Online]. Available: https://link.aps.org/doi/10.1103/PhysRev.121.584

[17] J. L. Vogl, "Radiative capture of protons by C12 and C13 below 700 kev," Ph.D. dissertation, California Institute of Technology, Jan. 1963.

[18] J. King, R. Azuma, J. Vise, J. Görres, C. Rolfs, H. Trautvetter, and A. Vlieks, "Cross section and astrophysical s-factor for the 13c(p, γ)14n reaction," *Nuclear Physics A*, vol. 567, no. 2, pp. 354–376, 1994. [Online]. Available: https://www.sciencedirect.com/science/article/pii/0375947494901546

[19] V. J. Zeps, E. G. Adelberger, A. García, C. A. Gossett, H. E. Swanson, W. Haeberli, P. A. Quin, and J. Sromicki, "Parity mixing of the 0^+-0^- i=1 doublet in ^{14}N," *Phys. Rev. C*, vol. 51, pp. 1494–1520, Mar 1995. [Online]. Available: https://link.aps.org/doi/10.1103/PhysRevC.51.1494

[20] G. Genard, P. Descouvemont, and G. Terwagne, "S-factor measurement of the 13c(p,γ)14n reaction in reverse kinematics," *Journal of Physics: Conference Series*, vol. 202, no. 1, p. 012015, jan 2010. [Online]. Available: https://dx.doi.org/10.1088/1742-6596/202/1/012015

[21] J. Skowronski, A. Boeltzig, G. F. Ciani, L. Csedreki, D. Piatti, M. Aliotta, C. Ananna, F. Barile, D. Bemmerer, A. Best, C. Broggini, C. G. Bruno, A. Caciolli, M. Campostrini, F. Cavanna, P. Colombetti, A. Compagnucci, P. Corvisiero, T. Davinson, R. Depalo, A. Di Leva, Z. Elekes, F. Ferraro, A. Formicola, Z. Fülöp, G. Gervino, R. M. Gesuè, A. Guglielmetti, C. Gustavino, G. Gyürky, G. Imbriani, M. Junker, M. Lugaro, P. Marigo, E. Masha, R. Menegazzo, V. Paticchio, R. Perrino, P. Prati, D. Rapagnani,

V. Rigato, L. Schiavulli, R. S. Sidhu, O. Straniero, T. Szücs, and S. Zavatarelli, "Proton-capture rates on carbon isotopes and their impact on the astrophysical $^{12}C/^{13}C$ ratio," *Phys. Rev. Lett.*, vol. 131, p. 162701, Oct 2023. [Online]. Available: https://link.aps.org/doi/10.1103/PhysRevLett.131.162701

[22] G. F. Ciani, L. Csedreki, J. Balibrea-Correa, A. Best, M. Aliotta, F. Barile, D. Bemmerer, A. Boeltzig, C. Broggini, C. G. Bruno, A. Caciolli, F. Cavanna, T. Chillery, P. Colombetti, P. Corvisiero, T. Davinson, R. Depalo, A. Di Leva, L. Di Paolo, Z. Elekes, F. Ferraro, E. M. Fiore, A. Formicola, Z. Fülöp, G. Gervino, A. Guglielmetti, C. Gustavino, G. Gyürky, G. Imbriani, M. Junker, I. Kochanek, M. Lugaro, P. Marigo, E. Masha, R. Menegazzo, V. Mossa, F. R. Pantaleo, V. Paticchio, R. Perrino, D. Piatti, P. Prati, L. Schiavulli, K. Stöckel, O. Straniero, T. Szücs, M. P. Takács, F. Terrasi, D. Trezzi, and S. Zavatarelli, "A new approach to monitor ^{13}C-targets degradation in situ for $^{13}C(\alpha, n)^{16}O$ cross-section measurements at luna," *The European Physical Journal A*, vol. 56, no. 3, p. 75, 2020. [Online]. Available: https://doi.org/10.1140/epja/s10050-020-00077-0

[23] G. F. Knoll, *Radiation detection and measurement; 4th ed.* New York, NY: Wiley, 2010. [Online]. Available: https://cds.cern.ch/record/1300754

[24] C. E. Rolfs and W. S. Rodney, *Cauldrons in the cosmos : nuclear astrophysics*, 1988.

[25] J. F. Ziegler, "Srim - the stopping and range of ions in matter," http://www.srim.org/, 2024, accessed: 2024-05-01.

[26] C. Iliadis, T. Schange, C. Rolfs, U. Schröder, E. Somorjai, H. Trautvetter, K. Wolke, P. Endt, S. Kikstra, A. Champagne, M. Arnould, and G. Paulus, "Low-energy resonances in 25mg(p, γ)26al, 26mg(p, γ)27al and 27al(p, γ)28si," *Nuclear Physics A*, vol. 512, no. 3, pp. 509–530, 1990. [Online]. Available: https://www.sciencedirect.com/science/article/pii/037594749090084Y

[27] G. Imbriani, H. Costantini, A. Formicola, A. Vomiero, C. Angulo, D. Bemmerer, R. Bonetti, C. Broggini, F. Confortola, P. Corvisiero, J. Cruz, P. Descouvemont, Z. Fülöp, G. Gervino, A. Guglielmetti, C. Gustavino, G. Gyürky, A. P. Jesus, M. Junker, J. N. Klug, A. Lemut, R. Menegazzo, P. Prati, V. Roca, C. Rolfs, M. Romano, C. Rossi-Alvarez, F. Schümann, D. Schürmann, E. Somorjai, O. Straniero, F. Strieder, F. Terrasi, and H. P. Trautvetter, "S-factor of $^{14}N(p, \gamma)^{15}O$ at astrophysical

energies□," *The European Physical Journal A - Hadrons and Nuclei*, vol. 25, no. 3, pp. 455–466, Sep. 2005, the astrophysical $S(E)$ factor of $^{14}\mathrm{N}(\mathrm{p},\gamma)^{15}\mathrm{O}$ has been measured for effective center-of-mass energies between $E_{\mathrm{eff}} = 119$ and 367 keV at the LUNA facility using TiN solid targets and Ge detectors. The data are in good agreement with previous and recent work at overlapping energies. R-matrix analysis reveals that due to the complex level structure of $^{15}\mathrm{O}$ the extrapolated $S(0)$ value is model dependent and calls for additional experimental efforts to reduce the present uncertainty in $S(0)$ to a level of a few percent as required by astrophysical calculations. [Online]. Available: https://doi.org/10.1140/epja/i2005-10138-7